Article

Transmission Electron Microscopy Reveals Propionic Acid-induced Alterations to Mitochondrial Morphology in SH-SY5Y Cells

Erin Buchanan[1], Caitlyn Mahony[1], Sophia Bam[1], Mohamed Jaffer[2], Sarah Macleod[1], Mignon van der Watt[1], Caron Jacobs[3] and Colleen O'Ryan[1]*

[1] Department of Molecular and Cell Biology, University of Cape Town, Cape Town, 7700, South Africa
[2] Electron Microscope Unit, University of Cape Town, Cape Town, 7700, South Africa
[3] Department of Pathology, Wellcome Centre for Infectious Diseases Research in Africa and IDM Microscopy platform, Institute of Infectious Disease and Molecular Medicine, University of Cape Town, Cape Town, 7700, South Africa
* Correspondence: colleen.oryan@uct.ac.za

Abstract: Mitochondrial dysregulation is implicated in numerous neurological disorders. Mitochondrial dynamics, including biogenesis, fusion and fission, are essential components of mitostasis which is modulated by complex regulatory mechanisms. Although expression studies are often used to investigate mitochondrial dynamics, these studies may be limited by the interdependent and temporal nature of mitostasis. Transmission electron microscopy (TEM) and cryogenic preparation methods provide a direct approach to examine mitochondrial ultrastructure in neurons. We investigated the utility of TEM to visualize mitochondrial morphological changes in SH-SY5Y cells treated with propionic acid (PPA). We examined whether morphological alterations were associated with differences in membrane potential or expression of biogenesis, fusion and fission genes. PPA induced a significant decrease in mitochondrial area ($p<0.01$ 5mM), Feret's diameter and perimeter ($p<0.05$ 5mM), and in area^2 ($p<0.05$ 3mM, $p<0.01$ 5mM) – consistent with a shift towards fission. Morphological changes were not associated with significant differences in mitochondrial membrane potential. However, we observed decreased gene expression of *NRF1* ($p<0.01$), *TFAM* ($p<0.05$), and *STOML2* ($p<0.0001$). These data support a disruption of the balance in dynamics to preserve function under stress. This demonstrates the utility of TEM to provide insight into mitochondrial dynamics and function which can inform targeted mechanistic investigations into neuropathology.

Keywords: mitochondrial; morphology; dynamics; fusion; fission; biogenesis; transmission electron microscopy; neuronal models; neuropathology; SH-SY5Y

1. Introduction

Mitochondria are integral players in diverse cellular functions beyond their canonical roles in energy production and biosynthesis. Mitochondrial metabolism is a key regulator of calcium signaling, metabolic and redox homeostasis, inflammatory signaling, epigenetic modifications and cellular proliferation, differentiation and programmed cell death [1]. In particular, mitochondrial metabolism is essential for the development, survival and function of neurons, and mitochondria are widely implicated in neurodevelopmental and neurodegenerative disorders [2–8]. Over the past decade, metabolic state has become well-established as a central regulator of neurogenesis, differentiation, maturation and plasticity [9–11]. More recently, mitochondrial morphology and dynamics have emerged as particularly important components of mitostasis, which refers to the dynamic processes that maintain the pool of healthy mitochondria. This has profound functional implications for neurodevelopment and neuropathology [12–14].

Mitochondrial dynamics are modulated by complex, interdependent pathways, ranging from mitochondrial biogenesis and bioenergetics to mitochondrial fission, fusion,

 doi:10.20944/preprints202211.0553.v1

transport and clearance [15,16]. A disruption to any of these integrated mechanisms impairs the maintenance of a healthy mitochondrial network, which is implicated in the mitochondrial dysfunction observed across numerous psychiatric, neurodegenerative and neurodevelopmental disorders [17,18]. Thus, improving our mechanistic understanding of the relationship between mitochondrial dynamics, morphology and function is a key target for ongoing research into neuropathology.

Quantifying RNA or protein expression is one of the most common approaches used to investigate the role of specific genes in response to mitochondrial stress. However, this approach can be limited by the multifaceted and temporally specific nature of the mechanisms that govern mitostasis. Furthermore, the differential expression of a limited number of mitochondrial genes is an indirect proxy to functional change. Thus, a more direct method to explore mitochondrial function and bioenergetics has been proposed [19,20]. Mitochondrial morphology is closely coupled to mitochondrial dynamics; the shape, connectivity and structure of mitochondrial cristae are essential for energy generation as well as mitochondrial- and cellular-survival [9,11]. Moreover, disparate components of mitostasis converge on alterations to mitochondrial morphology and could function as a useful endpoint of mitochondrial dysfunction to inform subsequent mechanistic studies.

The morphology of mitochondria can be directly visualized by transmission electron microscopy (TEM), which allows for the detailed examination of cellular ultrastructure. TEM yields insights into mitochondrial morphology, shape, and cristae structure at the resolution of single mitochondria as opposed to relying only on gene transcription, protein expression or parameters of mitochondrial function across cell populations [19,21,22]. Moreover, TEM can facilitate the study of interactions between mitochondria and other organelles like the endoplasmic reticulum and autophagosomes, which play a critical role in mitochondrial function and homeostasis [23–26]. However, TEM comes with some significant challenges that have historically limited its utility. Firstly, conventional electron microscopy sample preparation uses glutaraldehyde and osmium tetroxide to fix cells before dehydration using ethanol and acetone. These methods can lead to artefacts and distorted cellular membranes and organelles, including mitochondria [22]. Importantly, neuronal cells are particularly fragile cells and thus more vulnerable to damage during preprocessing using these standard techniques [27,28]. Secondly, TEM has often been employed as a qualitative rather than quantitative measurement of morphology. Qualitative data from individual images cannot yield sufficiently objective data to draw reliable mechanistic conclusions [19,29,30]. Nevertheless, as mitochondrial dynamics are increasingly implicated in neuropathology, there is a clear need to be able to directly, and quantitatively, investigate mitochondrial morphology in in vitro neuronal models.

Propionic acid (PPA) is widely used to model mitochondrial dysfunction in neurons and has been shown to disrupt mitochondrial membrane potential, biogenesis, and respiration in vitro [31–35]. PPA is known to impair neuronal metabolism and alter behavior in vivo and is an established animal model to study neurodevelopmental mechanisms involved in autism spectrum disorder (ASD) [36–44]. However, the effect of PPA on mitochondrial morphology and dynamics remains understudied. Hence, this study aimed to establish a method to quantitatively examine the effect of PPA on mitochondrial morphology, dynamics and function in SH-SY5Y cells.

First, we show that cryogenic sample preparation using high-pressure freezing and freeze substitution methods leads to minimal changes to cellular and mitochondrial structure compared to conventional sample preparation methods [45,46]. We develop a mitochondrial image analysis pipeline that automatically and objectively measures mitochondrial morphology using eight quantitative parameters [19,29,30,47]. Lastly, we use this workflow to investigate PPA-induced alterations to mitochondrial morphology and dynamics in the SH-SY5Y cell line. In addition, we explore whether mitochondrial morphology is associated with, or mechanistically explained by alterations to mitochondrial membrane potential or the expression of genes involved in biogenesis, fission and fusion. Together, our data illustrate the complexity of upstream regulatory mechanisms involved in

Preprints (www.preprints.org) | NOT PEER-REVIEWED | Posted: 30 November 2022 doi:10.20944/preprints202211.0553.v1

mitochondrial dynamics and emphasize the utility of TEM to explore mitochondrial morphology as a measurable, convergent endpoint of mitostasis in neurons.

2. Results

2.1 Cryogenic sample preparation preserves mitochondrial ultrastructure in neuronal-like cells

Conventional TEM sample preparation can induce artefacts due to protein aggregation or cross-linking which reportedly disrupts cellular ultrastructure. Notably, subcellular organelles in cells were shown to lose integrity following standard glutaraldehyde and formaldehyde-based fixation [28]. Therefore, we examined whether high-pressure freezing and freeze-substitution was better at preserving the ultrastructure of cellular organelles. We found that 3T3 cell samples prepared using conventional TEM sample preparation showed disrupted morphology with indistinct, spherical mitochondria without clearly defined cristae (Figure 1A). SH-SY5Y cells prepared using cryogenic techniques displayed less cellular distortion with a mixed population of homogenous-shaped, curved mitochondria with clearly visible cristae (Figure 1B). Thus, cryogenic methods were employed to investigate changes to mitochondrial morphology and dynamics in subsequent experiments.

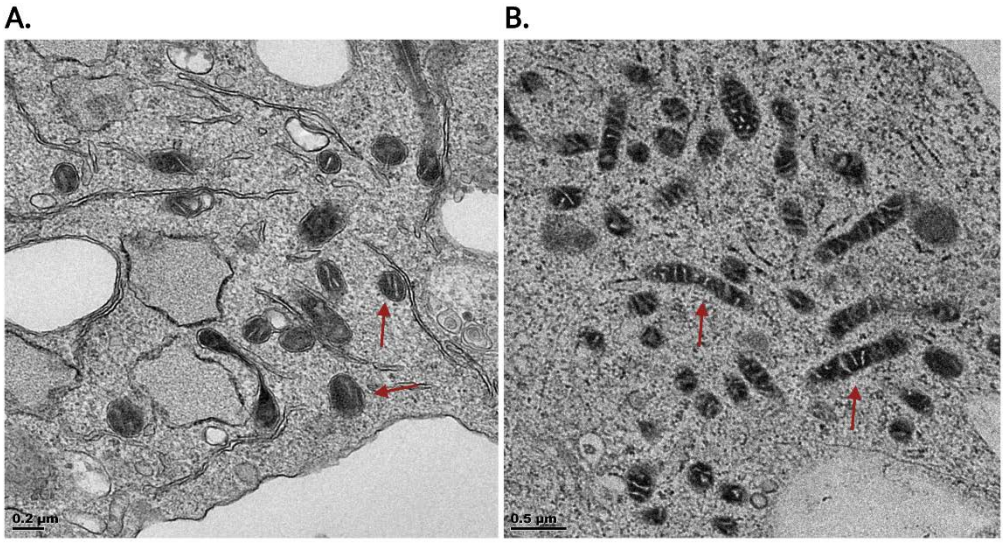

Figure 1: Cryogenic sample preparation techniques do not disrupt mitochondrial morphological architecture in the absence of propionic acid treatment. **A.** Representative transmission electron microscopy (TEM) image of control 3T3 cells using conventional preparation techniques. Mitochondria appear round and small, with cellular distortion and large vacuoles. **B.** Representative TEM image of control SH-SY5Y cells using cryogenic preparation techniques. The majority of mitochondria appear more elongated and display the expected morphology. Red arrows indicate mitochondria.

2.2 Propionic acid remodels mitochondrial morphology

To induce mitochondrial stress, SH-SY5Y cells were treated with PPA, administered using sodium propionate (NaP) (3mM or 5mM). Samples underwent cryogenic sample preparation techniques including high-pressure freezing and freeze substitution prior to TEM (Figure 2A). We developed an automated mitochondrial image analysis pipeline to measure eight morphological parameters. We found that four of these parameters were significantly altered by PPA: area^2, area, perimeter and Feret's diameter (Figure 2B-E). The area^2 was significantly decreased at both 3mM and 5mM PPA treatment ($p<0.05$ and $p<0.01$, respectively) (Figure 2B), whilst the area ($p<0.01$), perimeter ($p<0.05$) and Feret's diameter ($p<0.05$) were significantly decreased in the 5mM treatment group compared to controls (Figure 2C-E). The significant decrease in area and perimeter suggests that cells treated with 5mM PPA have smaller, rounder mitochondria and that these mitochondria

 doi:10.20944/preprints202211.0553.v1

are not as elongated as those in control cells (Figure 2F). This is also consistent with the significant decrease in Feret's diameter, which is an independent parameter showing that the longest distance between the edges of the particles is decreasing. These data may represent two possible scenarios: either PPA upregulates fission or downregulates fusion leading to existing mitochondria becoming smaller; or new, smaller mitochondria are produced by an increase in mitochondrial biogenesis. These two scenarios cannot be distinguished using TEM, therefore we explored additional parameters to examine the underlying mechanisms of mitostasis.

2.3 Mitochondrial membrane potential is not altered under propionic acid stress

To investigate whether the morphological changes corresponded with mitochondrial membrane potential changes, MitoTracker Red and DAPI staining were used to assess membrane potential at 3mM and 5mM PPA treatment after both 24 and 48 hours (Figure 3A). We expanded the time of PPA treatment since mitochondrial function may respond dynamically to different degrees of stress. There were no significant differences in the average MitoTracker intensity at either time point (Figure 3B and D) which may suggest that the morphological alterations observed with PPA indicate an efficient mitochondrial compensatory mechanism. The latter would ultimately preserve the function of the mitochondrial cellular network as a whole. Noteworthy, there was a spread of individual values across the 18 technical repeats captured for each treatment condition, which indicates a high variability between different cell populations (Figure 3C and E). This highlights the utility of parameters that can be measured at the resolution of individual mitochondria rather than variables that measure the mean mitochondrial response across whole cells and cell populations.

2.4 Propionic acid alters transcriptional regulators of mitostasis and dynamics

In the absence of significant differences in mitochondrial membrane potential, we examined whether the observed morphological remodeling in response to PPA treatment was associated with the differential expression of seven key regulators of mitochondrial dynamics and mitostasis. We quantified gene expression of Nuclear Respiratory Factor (*NRF1)*, NFE2-Like BZIP Transcription Factor (*NFE2L2)*, Mitochondrial Transcription

Preprints (www.preprints.org) | NOT PEER-REVIEWED | Posted: 30 November 2022 doi:10.20944/preprints202211.0553.v1

Factor 1 (*TFAM)*, Stomatin-Like Protein 2 (*STOML2)*, Dynamin-Related Protein 1 (*DRP1)*, Mitofusin 1 (*MFN1)* and Mitofusin 2 (*MFN2)* at 3mM and 5mM PPA after 24 hours.

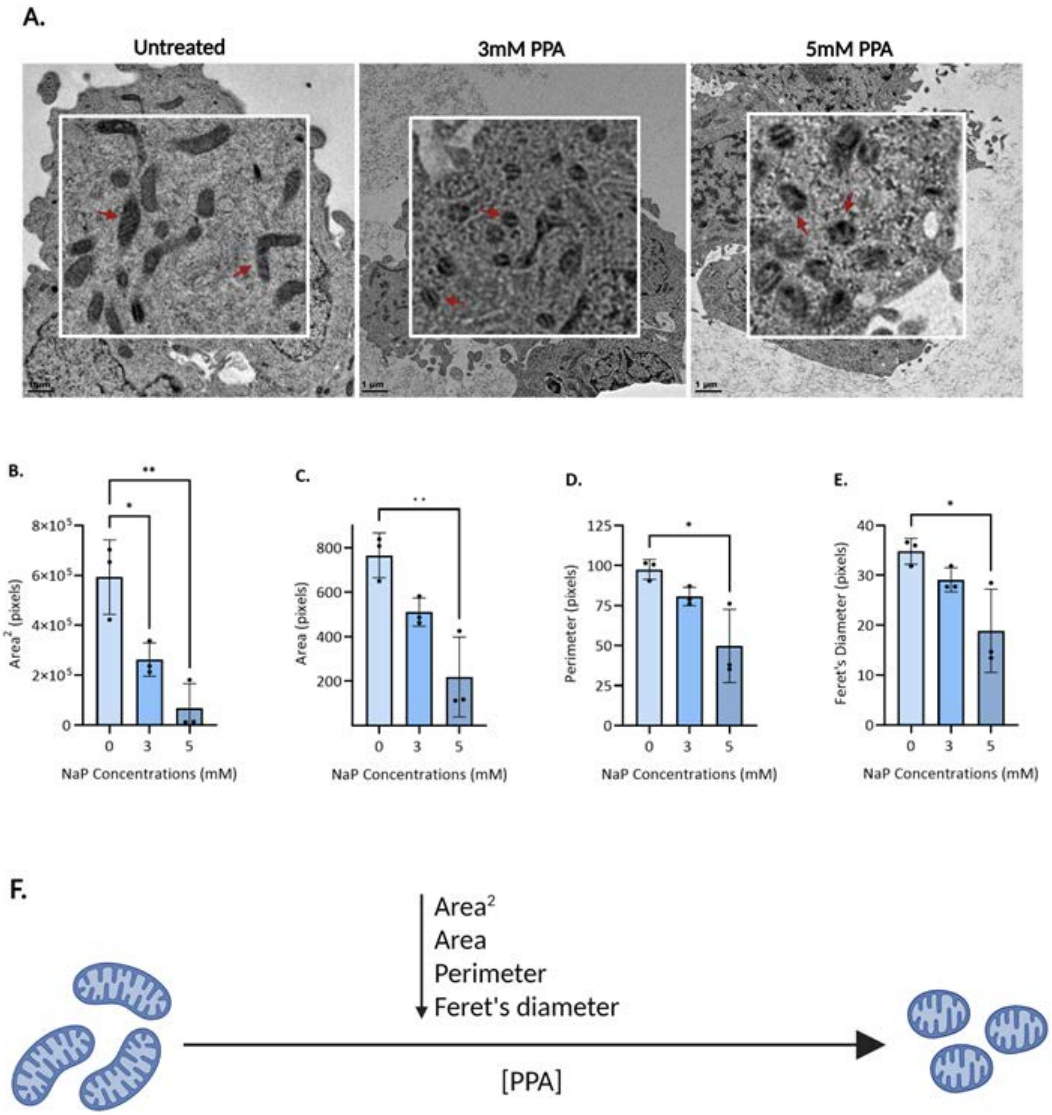

Figure 2: Propionic acid (PPA) remodels mitochondrial morphology. **A.** Representative transmission electron microscopy (TEM) images show a decrease in mitochondrial size with mitochondria becoming smaller and rounder with increasing PPA treatment; untreated, 3mM and 5mM respectively. Red arrows indicate mitochondria. **B. – E.** SH-SY5Y cells treated with PPA for 24 hours underwent preparation for TEM and results were analyzed using Fiji/ImageJ. Four of the eight parameters showed significant differences between control (untreated, 0mM PPA) and treated (3mM and 5mM PPA) cells. **B.** Area², **C.** Area, **D.** Perimeter, **E.** Feret's Diameter. **F.** Diagram summarizing the change in morphology and decrease in parameters as mitochondria become smaller. Significant differences were identified using one-way ANOVA (control compared to treatments) and Dunnett's test for multiple comparisons ($p<0.05$). Bars represent mean parameters; error bars represent standard deviation. The data shown represents n=3 biological repeats; a total of 266 images were analyzed; * indicates $p<0.05$, ** indicates $p<0.01$. Diagram made using BioRender.com.

We observed a significant decrease in the expression of the central mitogenesis regulators, *NRF1* and *TFAM* ($p<0.01$ and $p<0.05$, respectively) after 24 hours of 3mM and 5mM PPA treatment (Figure 4A, C). *NRF1* had a 2.6- (3mM) and 3- (5mM) fold change while *TFAM* had a 1.9- (3mM) and 2.2- (5mM) fold change. The central redox-responsive antioxidant gene, *NFE2L2,* was not altered under any concentration of PPA although there

Preprints (www.preprints.org) | NOT PEER-REVIEWED | Posted: 30 November 2022 doi:10.20944/preprints202211.0553.v1

was a dose-dependent decreasing trend in expression (Figure 4B). The expression of *STOML2*, which is thought to be involved in fusion, mitophagy and potentially in biogenesis, was significantly decreased at both 3mM (2.4-fold change) and 5mM (2.8-fold change) PPA ($p<0.0001$) (Figure 5A). However, we found no significant differences in the expression of the fusion genes *MFN1/2* or the fission gene *DRP1* (Figure 5B-D). Together, the significantly decreased expression of *NRF1*, *TFAM* and *STOML2* is consistent with a reduction in mitochondrial biogenesis and decreased mitochondrial fusion. While this may not necessarily reflect transcriptional changes over the preceding 24 hours, these data may suggest that the decreased size of mitochondria observed with TEM is not attributed solely to increased mitochondrial biogenesis, but to a dysregulation of the balance between mitochondrial fission, fusion and biogenesis under PPA stress.

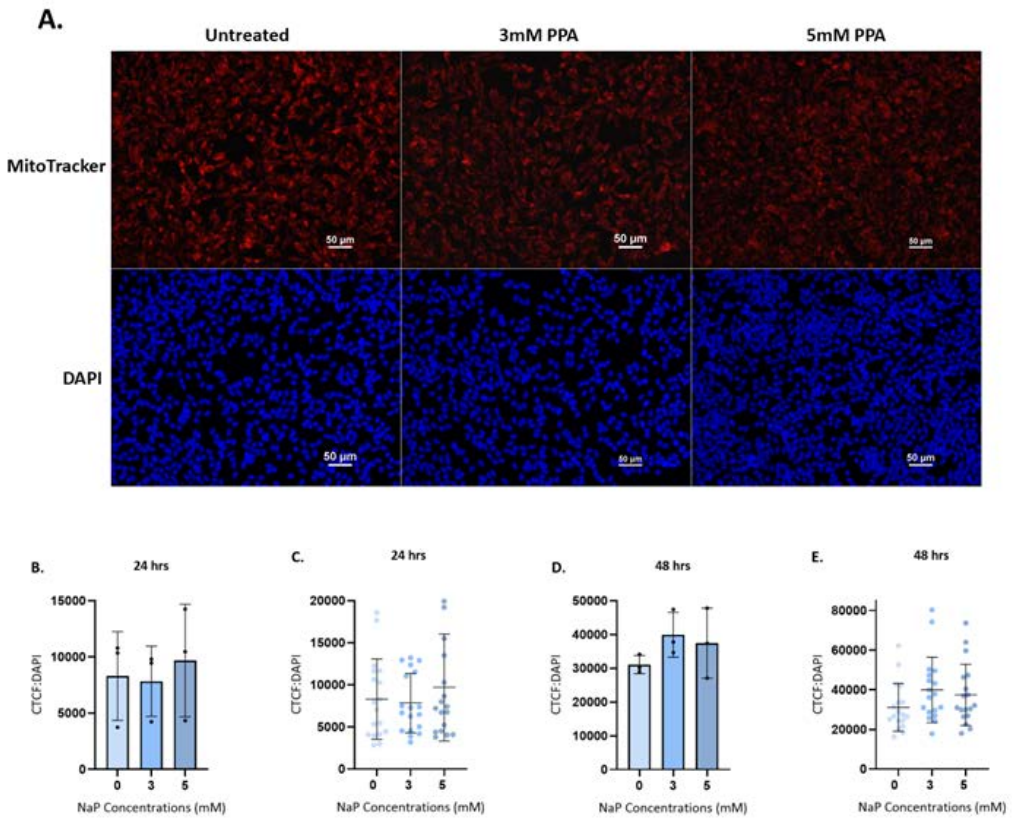

Figure 3: Mitochondrial membrane potential remains unchanged after propionic acid (PPA) treatment. **A.** Representative images of MitoTracker and DAPI staining of cells after 24 hours PPA treatment. Images were captured at 20x magnification using a Nikon TiE Inverted Fluorescence Microscope. Treatments were performed in duplicate; each well was visualized at three regions of interest and the experiment was repeated in three independent biological repeats**. B. – E.** Membrane potential, represented by average CTCF:DAPI, was measured using MitoTracker Red and DAPI in SH-SY5Y cells untreated (0mM PPA) and cells treated with 3 and 5mM PPA for 24 hours (B., C.) or 48 hours (D, E.). No significanct differences were found between the controls and treated samples. The spread of values in each sample shown in C. and E. shows the variability of membrane potential within cell populations. Significant differences were tested using one-way ANOVA (control compared to treatments) and Dunnett's test for multiple comparisons ($p<0.05$). Bars represent the mean CTCF:DAPI; error bars represent standard deviation. The data shown represents n=3 biological repeats.

Preprints (www.preprints.org) | NOT PEER-REVIEWED | Posted: 30 November 2022 doi:10.20944/preprints202211.0553.v1

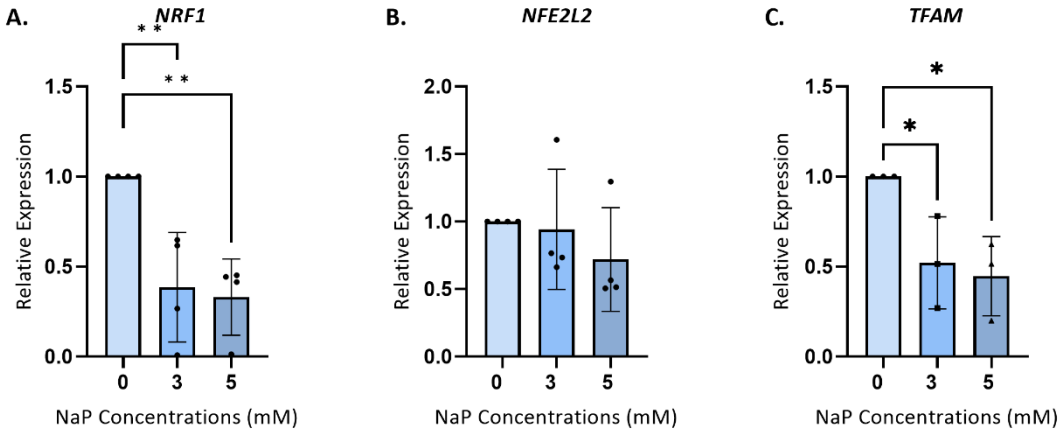

Figure 4. Propionic acid induces a transcriptional downregulation of mitochondrial biogenesis after 24 hours. Relative quantification of **A.** *NRF1*, **B.** *NFE2L2* and **C.** *TFAM* expression was performed using RT-qPCR and normalized to *B2M*. Significant differences were tested using one-way ANOVA (control compared to treatments) and Dunnett's test for multiple comparisons ($p<0.05$); * indicates $p<0.05$, ** indicates $p<0.01$. Bars represent the mean expression; error bars represent standard deviation. The data shown represents n=4 (*NRF1*, *NFE2L2*) and n=3 (*TFAM*).

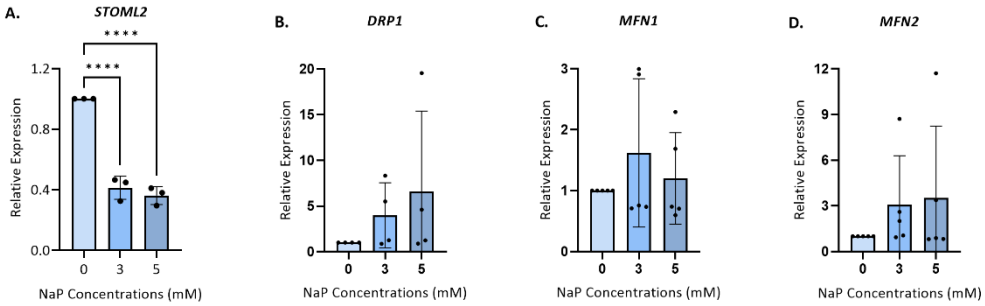

Figure 5: Fusion and fission gene expression is altered by propionic acid. Relative quantification of **A.** *STOML2*, **B.** *DRP1*, **C.** *MFN1* and **D.** *MFN2* expression was performed using RT-qPCR and normalized to *B2M*. Significant differences were tested using one-way ANOVA (control compared to treatments) and Dunnett's test for multiple comparisons ($p<0.05$); **** indicates $p<0.0001$. Bars represent the mean expression; error bars represent standard deviation. The data shown represents n=3 (*STOML2*), n=4 (*DRP1*) and n=5 (*MFN1*, *MFN2*) biological repeats.

3. Discussion

Mitochondrial dysfunction has been implicated in multi-systemic disorders ranging from metabolic, cardiovascular and muscular diseases to neurological disorders [1,14]. Numerous neurodevelopmental and neurodegenerative disorders are linked to mitochondrial dysfunction, emphasizing the importance of these organelles throughout the brain's lifespan. These disorders include Parkinson's and Alzheimer's disease and ASD [48,49]. However, accessing brain tissue to study these diseases, particularly at the mechanistic level, is difficult, thus cell model systems serve as a necessary alternative.

PPA and other PPA derivatives are reported to recapitulate an "ASD-like" phenotype in animal and cell culture models [39,44,50]. Moreover, PPA treatment reflects the molecular disruptions previously observed in a South African ASD cohort. Here, significant differential methylation of Propionyl-CoA Carboxylase Subunit Beta (*PCCB*) was associated with ASD [51]. Differential methylation of *PCCB* alters gene expression and changes the function of propionyl-CoA carboxylase (PCC) [52,53]. Disruptions to PCC function prevent the breakdown of PPA, causing it to accumulate to toxic levels. For example, mitochondrial dysfunction caused by toxic levels of PPA is observed in metabolic disorders

 doi:10.20944/preprints202211.0553.v1

caused by mutations in PCC, like propionic acidemia [54]. Therefore, using the PPA model for mitochondrial dysfunction in neurons may yield insight into ASD aetiology.

In this study, we explored the feasibility of using TEM to view mitochondrial morphological changes. Importantly, TEM must be used appropriately to maximize its utility. Artefacts from sample preparations can result in erroneous images and subsequent analyzes. Thus, cell-specific sample preparation techniques should be carefully optimized to ensure the preservation of mitochondrial ultrastructure. We found that conventional TEM sample preparation using glutaraldehyde and osmium tetroxide significantly disrupted mitochondrial ultrastructure in 3T3 cells (Figure 1A), which demonstrated that this approach was ill-suited to study mitochondrial dynamics, particularly in fragile neuronal-like cells. Cryogenic sample preparation allows for the simultaneous immobilization of cellular components and decreased formation of artefacts, which together better preserve neuronal architecture [55]. Consistent with this, we observed that neuronal-like SH-SY5Y cells displayed intact subcellular organelles and elongated mitochondria with well-defined cristae (Figure 1B). This highlights the utility of cryogenic preparation approaches to study mitochondrial morphology in neuronal cell models.

While it is increasingly evident that quantitative measures are essential for the objective analysis of TEM data, there is still no consensus regarding which specific parameters should be measured to confirm mitochondrial morphology changes. Based on previous studies that have quantitatively examined mitochondrial morphology [19,29,30], we developed an automated mitochondrial image analysis pipeline that measured eight morphological parameters, namely, area, area^2, form factor, aspect ratio, perimeter, circularity, Feret's diameter and roundness. Of these, PPA significantly decreased area, area^2, perimeter and Feret's diameter. This suggests that mitochondria became smaller and rounder, which is consistent with previous studies showing that mitochondrial area decreased after PPA-induced mitochondrial stress [34]. These morphological features may be indicative of mitochondrial fission, a process essential to separate damaged components from the mitochondrial network to facilitate their degradation by mitophagy [56]. On the other hand, a decrease in average mitochondrial size can result from the upregulation of biogenesis, which produces small nascent mitochondria. An increase in either fission or biogenesis represents compensatory responses to maintain mitostasis in response to mitochondrial stress.

TEM images do not provide direct evidence about which gene regulatory mechanisms underlie morphological changes. Therefore, we examined mitochondrial membrane potential to determine whether the remodeling in mitochondrial morphology was associated with perturbations to mitochondrial function. Mitochondrial membrane potential is recognized as an indicator of mitochondrial function. No significant differences in mitochondrial membrane potential were detected following 3mM or 5mM PPA treatment (Figure 3B-E), which indicates that the morphological alterations observed with TEM may represent compensatory responses that effectively maintain the health of the mitochondrial network. Nonetheless, a slight increasing trend in membrane detection was visible at 24 hours (5mM) and 48 hours (3mM and 5mM) post-PPA treatment (Figure 3C, E). Previous studies have shown that low PPA levels increase the rate of mitochondrial oxidative phosphorylation as PPA is metabolized to succinyl-CoA, which fuels the TCA cycle [50]. This increase in mitochondrial electron chain transport activity is marked not only by increased mitochondrial membrane potential but also an increase in mitochondrial ROS production. The latter exerts detrimental effects on cellular metabolism and function. Congruent with this, Fillier et al. (2022) reported that short chain fatty acids, including propionate, significantly increased MitoTracker signal intensity after 72 hours. Notably, this was associated with increased mitochondrial fragmentation and hyperfusion and decreased ATP production and basal and maximal mitochondrial respiration [57].

On the other hand, Kim et al. (2019) reported significantly decreased mitochondrial membrane potential in SH-SY5Y cells after four hours under PPA stress. These conflicting results suggest a loss of mitochondrial membrane potential immediately following PPA administration before compensatory responses like metabolic remodeling, mitogenesis,

 doi:10.20944/preprints202211.0553.v1

fission and fusion take effect. Alternatively, the conflicting data may be indicative of differential responses to PPA and NaP, which mediates its effects via both propionate and PPA in solution [50]. Moreover, we also observed discrepancies in MitoTracker intensity across different cell populations under the same conditions (Figure 3). It has previously been shown that the degree of MitoTracker intensity is associated with distinct metabolic phenotypes within the same cell population [58]. This may be particularly true for cell populations that are undergoing dynamic metabolic remodeling in response to mild mitochondrial stress. Given that the morphological changes observed at the resolution of individual mitochondria were not associated with significant changes to mitochondrial function across the mitochondrial network, we next explored whether PPA induced mitochondrial compensation via biogenesis, fission, or fusion.

Fillier et al. (2022) proposed that the increase in MitoTracker intensity in SCFA-treated SH-SY5Y cells was indicative of increased mitochondrial mass due to the upregulation of mitogenesis in response to impaired energy homeostasis and increased oxidative stress. Moreover, PPA has previously been reported to increase protein expression of PGC-1α and mitochondrial DNA (mtDNA) copy number in SH-SY5Y cells after 24 hours and 72 hours respectively [34]. Therefore, we examined the expression of several key genes involved in mitochondrial biogenesis. *NRF1* and *TFAM* are two central regulators of mitogenesis that function downstream of PGC-1α to upregulate mtDNA replication. This pathway is activated by cAMP and AMPK signaling, which is sensitive to energy depletion and metabolic stress. We also examined *NFE2L2*, which is a redox-responsive regulator of mitochondrial biogenesis to determine whether the effects of PPA may be mediated by oxidative stress.

While *NFE2L2* expression remained unchanged after 24 hours at 3–5mM PPA treatment, we found a consistent decrease in both *NRF1* and *TFAM* expression across both concentrations (Figure 4A, C). These data are in line with previous studies in human colon cancer cells showing that PPA decreases *NRF1* mRNA expression after 22 hours, which was associated with ATP depletion and increased ROS [59]. This contrasted with *TFAM* expression, which peaked at 8.5 hours but returned to baseline levels after 22 hours. On the other hand, prior work in SH-SY5Y cells has also shown a significant decrease in *TFAM* mRNA expression after 24 hours of PPA stress [34]. Interestingly, these authors found that TFAM protein expression was significantly upregulated after 24 hours, and this was associated with significantly increased mtDNA copy number after 72 hours. Together, these data suggest that mtDNA replication may be transcriptionally upregulated at earlier time points, before changes in protein expression, mtDNA copy number and membrane potential are observed. Nevertheless, our data show that the mRNA expression of three transcriptional regulators of biogenesis is consistently decreased at the time point of interest. This data may suggest a PPA-induced downregulation of mitochondrial biogenesis on a transcriptional level.

The genes *STOML2, DRP1, MFN1* and *MFN2* are some of the central regulators of mitochondrial fission, fusion and dynamics [60–62]. Moreover, both *STOML2* and *MFN2* were previously found to be differentially methylated in an ASD cohort [63] while several independent studies reported alterations to these transcription factors in response to mitochondrial stress [64–67]. We found no significant differences in gene expression of *MFN1*, *MFN2* or *DRP1* after 24 hours of PPA treatment. This could indicate that there are no changes in the transcriptional regulation of the direct factors involved in mitochondrial fusion and fission. Alternatively, it is possible that similar to the regulation of mitogenesis, transcriptional dysregulation precedes the alterations to mitochondrial morphology that we observe after 24 hours. Moreover, each of these genes is also regulated by post-transcriptional mechanisms that control protein activity. DRP1 activity is regulated by phosphorylation by calcium/calmodulin-dependent protein kinase-II (CaMKII), while DRP1 degradation is regulated by ubiquitylation and SUMOylation [68]. DRP1 and MFN1/2 are also GTPases, and their activity may be influenced by the rate of GTP production in the mitochondria [69]. Therefore, while the expression of these genes remained constant, this may not directly translate into unaltered activity [70,71].

 doi:10.20944/preprints202211.0553.v1

On the other hand, *STOML2* expression was significantly decreased at 3mM and 5mM PPA treatment. While the role of *STOML2* in mitochondrial dynamics remains elusive, there is evidence to suggest that it plays a role in mitochondrial fusion, metabolism and mitophagy. STOML2 is involved in maintaining coupled mitochondrial respiration and the formation of respiratory chain complexes [72,73] and has been shown to profoundly alter the metabolic profile and proliferative capacity of cancer cells [74]. Moreover, independent studies have demonstrated an interaction between STOML2 and PINK1 that modulates mitophagy [75,76]. Notably, it has been reported that STOML2 directly interacts with and stabilizes MFN2 and another central fusion gene, OPA1 [60,77]. The decrease in *STOML2* expression observed in response to PPA may render these fusion proteins more susceptible to degradation by ubiquitin and proteasome-dependent pathways [62], thereby disrupting the balance between fission and fusion. While the precise role of STOML2 in the morphological response to PPA is unclear, it is possible that the decreased *STOML2* expression (Figure 5A) contributes to a decrease in fusion, leading to an upregulation of fission and the subsequent decrease in mitochondrial size.

Collectively, the data presented above highlights the complexity and temporally specific mechanisms that regulate mitochondrial morphology, and how challenging these mechanisms are to study. To examine gene expression, specific target genes in a pathway first need to be identified. However, our data show that genes within the same pathway do not respond homogeneously to the same stress. In fact, previous studies have shown that different genes in the same pathway can display different temporal response profiles [34,59]. In addition, there are complex post-transcriptional mechanisms that confound the relationship between gene transcription and function. Proteomic studies may yield some insight into the effect of post-translational modifications and protein function, but this also presents challenges, including low-throughput methods, high signal-to-noise ratios and poor resolution.

In this context, using TEM to study mitochondrial morphology has great potential to address fundamental questions about the relationship between mitochondrial dynamics and function, and how this impacts disease. Most significantly, TEM provides a direct way to measure mitochondrial morphology, which serves as a convergent endpoint parameter for disruptions to mitochondrial function and dynamics [66]. TEM cannot only support data obtained from gene and or protein expression studies but can also provide novel insight into the relationship between gene function and mitochondrial morphology [33,34]. TEM and other visualization tools may provide valuable insight into endpoint mitochondrial function that can be used to inform subsequent research questions and targeted mechanistic investigations. In a neuroscience context, this is especially relevant for the study of the pleiotropic neuropathologies that are associated with mitochondrial dysfunction. Ultimately, our data highlight the utility of imaging techniques to provide insight into the functional outcome of the complex interplay between gene expression, protein modifications, and protein activity that governs mitostasis.

4. Materials and Methods

4.1 Cell Culture

The SH-SY5Y cell line (ECACC, 94030304-1VL) was purchased from Sigma-Aldrich. SH-SY5Y cells were grown in 25cm^2 flasks in Dulbecco's Modified Eagle Medium/Nutrient Mixture F-12 (DMEM/F-12) with L-Glutamine (SC09411, ScienCell) supplemented with 20% Fetal Bovine Serum (FBS) (10493106, ThermoFisher Scientific) and 1% Penicillin-Streptomycin (P4333-20ML, Sigma-Aldrich) at 37°C, 5% CO_2. Cells were sub-cultured to 80% confluency using 0.05% Trypsin-EDTA (15400054, ThermoFisher Scientific), centrifuged at 300g and seeded at approximately 7x10^{5}cells/ml. All experiments were done on undifferentiated SH-SY5Y cells between passages 19–22. PPA was administered in the form of NaP. NaP powder (CAS number 137-40-6, chemical formula $C_3H_5NaO_2$, P5436-100G, Sigma-Aldrich) was dissolved in warm MilliQ water to a concentration of 1M and stored at 4°C. This 1M PPA solution was diluted in serum-free media (DMEM/F-12 with

 doi:10.20944/preprints202211.0553.v1

L-Glutamine) on the day of treatment to 3mM and 5mM PPA. Treatment concentrations for all experiments were no PPA (untreated, control), 3mM and 5mM PPA. Experiments were done in a minimum of three biological replicates. 3T3 mouse fibroblast cells with GFP-tubulin were kindly provided by Dr A Savulescu from the University of Cape Town. Cells were grown in DMEM-F12 with 1:10 Glutamax (31765027, Gibco) supplemented with 10% FBS. Cells were grown in the same conditions and sub-cultured using the same protocols as described above.

4.2 Transmission Electron Microscopy

4.2.1 Conventional sample preparation

Cells were grown in 75cm^2 flasks for 48 hours and routine sub-culturing protocol (described above) was followed to collect cell pellets. The protocol used was adapted from the Low Viscosity Embedding Media Spurr's Kit protocol (14300, Electron Microscopy Sciences) with the following modifications: Primary fixation was performed using 2.5% glutaraldehyde in 1X PBS overnight at 4˚C. After washing the pellets in 1X PBS, 1% osmium tetroxide in 1X PBS was used for secondary fixation for one hour at room temperature. En-bloc staining was done using 1% uranyl acetate for 30 minutes. Cells were washed in 1X PBS before serial dehydration with 30, 50, 90, 100% ethanol and 100% acetone was used for final dehydration. Samples were then infiltrated beginning with 2:1 resin:acetone for eight hours, 3:1 resin:acetone overnight, 10:1 resin:acetone for eight hours and 100% resin overnight. Infiltration using 100% resin was repeated for two hours followed by polymerization at 60˚C for 48 hours.

4.2.2 Cryogenic sample preparation

SH-SY5Y cells were seeded at 5.5 x 10^{5}cells/ml in 25cm^2 flasks and grown for 24 hours. PPA treatments were added to the flasks before incubating for 24 hours. Routine mammalian tissue sub-culturing protocol (described above) was followed to collect cell pellets. The cell pellets were resuspended in 100µl 2.5% glutaraldehyde, 1x PBS and stored at 4°C until processing. SH-SY5Y cells were briefly centrifuged to pellet the cells and remove the 2.5% glutaraldehyde, 1x PBS solution. Pellets were resuspended in 4% agarose gel made with distilled water (1:1 ratio agarose to pellet volume). Agarose slices were placed onto grids on a flat planchette and covered with 1-hexadecene before high-pressure freezing. Samples were freeze substituted at -90°C for 24 hours in 100% dry acetone. This was followed by raising the temperature to -80°C and adding a solution of 1% osmium tetroxide and 0.1% glutaraldehyde. Samples were kept at -80°C for 24 hours. Following this, the temperature was gradually increased to room temperature over multiple days: from -80°C to -50°C for 24 hours, to -30°C for 24 hours, to -10°C for 24 hours and finally to room temperature.

4.2.3 Infiltration, staining and microscopy

Following on after both conventional and cryogenic sample preparation, samples were infiltrated with resin, and ultrathin sections (~100nm) were cut with a Leica Reichert UltracutS Ultramicrotome (Leica Microsystems). Sections were stained with 2% uranyl acetate and lead citrate. Samples were viewed using a FEI Tecnai 20 transmission electron microscope (ThermoFisher (formerly FEI), Eindhoven, Netherlands) operating at 200kV (Lab6 emitter) and fitted with a Tridiem energy filter using a Gatan CCD camera (Gatan, UK).

4.2.4 Image analysis

A minimum of 24 images were captured per technical replicate with a total of 266 images overall. The Region of Interest (ROI) Macro and the Mitochondrial Macro were used to analyze all images. The Mitochondrial Macro was based on published methods [19,29,30] and allowed for the semi-automated batch processing of TEM images in Fiji/ImageJ [78]. Briefly: Images were inverted and preprocessed using a rolling ball background subtraction (radius of 60 pixels) and a FFT bandpass filter using upper and lower bounds of 60 and 8 pixels, respectively, and vertical line suppression with 5% tolerance of direction. The processed images were automatically thresholded using the Maximum Entropy

Preprints (www.preprints.org) | NOT PEER-REVIEWED | Posted: 30 November 2022 doi:10.20944/preprints202211.0553.v1

algorithm and binary masks generated. Image regions were extracted correlating with manually selected ROIs in unprocessed TEM images, featuring mitochondria and excluding plasma membrane and other regions of high contrast. For each extracted ROI, binary particles greater than 600 pixels were analyzed and particle area, perimeter, major and minor axes, Feret's diameter, circularity, and roundness were measured using the Fiji/ImageJ built-in measurement function. From these, particle aspect ratio (the ratio of major and minor axis), and form factor (FF), where FF = perimeter^2 / 4*pi x* area, as per Merrill, Flippo and Strack (2017), were calculated. On average, approximately 5 600 particles were analyzed for each PPA treatment, and approximately 17 000 particles were analyzed overall (data not shown).

4.3 MitoTracker Assay

SH-SY5Y cells were seeded in a 24-well plate at 2.5–3 x 10^5 and 5–8 x 10^4cells/well for 24 and 48 hour treatments, respectively. PPA treatments were administered in duplicate for both 24 and 48 hours. The PPA-treated SH-SY5Y cells were stained with 250nM MitoTracker® CMXRos (ThermoFisher Scientific, M7512) in serum-free media for 45 minutes at 37°C. After incubation, the cells were rinsed twice with 1X PBS. Cells were fixed with 4% paraformaldehyde (Inqaba Biotechnical Industries, SCH PA00950500) for 25 minutes, permeabilized with 0.5% Triton-X 100 (Inqaba Biotechnical Industries, GLS GD6826-100ML) for 25 minutes, and counterstained with 250nM DAPI (Biocom Africa, #422801) for 1 hour at 4°C. Finally, cells were rinsed twice with 1X PBS and mounted in 1X PBS for visualization with a Nikon Ti-E inverted fluorescence microscope equipped with the Nikon C-HGFIE Intensilight mercury-fiber illuminator and controlled by NIS-Elements AR imaging software v5.21.01. For each technical repeat, bright-field and fluorescent images were captured in triplicate with a DS-Fi2 color camera using a 20X S Plan Fluor objective (NA=0.70), using standardized conditions as follows. DAPI fluorescence was visualized using the Chroma DAPI Filter Set #49000 (Ex/Em = 320-380nm/ 435-485nm) at 1x analogue gain and 100-400 ms exposure. MitoTracker fluorescence was visualized with the Chroma Texas Red Filter set #49008 (Ex/Em = 540-580nm/ 590-670nm) at 1-1.4x analogue gain 800-1000 ms exposure. Raw 24-bit images were saved as .jpg files prior to image processing and analysis.

Image analyses were performed using Fiji/ImageJ to quantify fluorescence intensity [78]. Images were converted to 8-bit images and preprocessed with the rolling ball background subtraction (radius of 50 pixels). Images were then duplicated, and the duplicated image was binarized using the IsoData algorithm to set standardized thresholds for each repeat. Nuclei were counted after applying watershed to binarized DAPI images, filtering for a size between zero and infinity and a circularity between zero and one. The non-binarized MitoTracker images were measured for area, integrated density and mean grey value. Background fluorescence was calculated using the mean grey value across five manually selected representative background regions for each image. Fluorescent intensity was quantified as corrected total cell fluorescence (CTCF) and normalized by cell count, where CTCF = Integrated Density – (Fluorescence Area x Mean Fluorescence of background readings) [79].

4.4 RNA Extraction

The SH-SY5Y cells were grown in a six-well plate at a density of 0.3 x 10^6cells/ml for 24 hours before treatment. RNA was extracted from SH-SY5Y cells using the Quick-RNA™ Miniprep (ZR R1055, Zymo Research) protocol with minor modifications: 300µl of RNA lysis buffer was added to each well before scrapping and in the final step each sample was eluted in 30µl DNase/RNase-free water. The quantity and quality of all samples were checked using the NanoDrop ND-1000 UV-Vis Spectrophotometer.

4.5 Quantitative Real-Time PCR (RT-qPCR)

The cDNA synthesis was performed using the Tetro™ cDNA Synthesis Kit (BIO-65043, Meridian Bioscience) following the manufacturer's instructions with some modifications. Total RNA between 0.7-1µg was used to synthesize cDNA in a 20µl reaction.

 doi:10.20944/preprints202211.0553.v1

Primers were selected from previously published papers ([80–86], Table S1) and their accompanying probes were designed using the Integrated DNA Technologies' PrimerQuest Tool. All genes of interest were normalized to the nuclear gene *B2M*. Gene expression of *STOML2, NRF1, NFE2L2* and *TFAM* was measured using RT-qPCR. The master mix included LUNA Taq polymerase (M3003L, New England Biolabs), 10μM forward and reverse primer, cDNA and PCR-grade water to make up a final volume of 10μl per reaction. Rotor-Gene Q 6-plex (QIAGEN RG – serial number: R0618110) was used to perform RT-qPCR with the following cycling conditions: 95°C for 1 min, followed by 40 cycles of 95°C for 10s, 60°C for 30s, and 72°C for 10s for *NRF1* and *TFAM*. *NFE2L2* amplification was conducted as follows: 95°C for 1 min, followed by 40 cycles of 95°C for 10s, 60°C for 30s and 72°C for 10s, acquiring at both 60°C and 72°C for the green. *STOML2* amplification was conducted as follows, 95°C for 10 min, followed by 40 cycles of 95°C for 15s and 92°C for 30s.

Gene expression of the fission and fission genes (*DRP1*, *MFN1/2*) were measured in a multiplex TaqMan assay. Luna Universal Probe qPCR Master Mix (M3004S, New England Biolabs) was used according to the manufacturer's instructions with minor modifications. The multiplex RT-qPCR master mix included 1X LUNA Taq polymerase, 10μM of forward and reverse primers, 10μM of probes, cDNA and PCR-grade water to make up a final volume of 20μl per reaction. Amplification for the fission and fusion genes was performed with the following cycling conditions: 95°C for 60s, followed by 40 cycles of 95°C for 15s, 63°C for 30s and 72°C for 10s, acquiring at both 63°C and 72°C for the orange, red, green and yellow channels. All cDNA samples were amplified in triplicate with a standard curve in 10-fold dilution series. The cycling threshold (Ct) standard deviation within the triplicate samples was below 0.5. Relative gene expression was calculated using the $2^{-\Delta\Delta Ct}$ method [87].

4.6 Statistical Analysis

Data sets are shown as the mean and standard deviation of at least three independent samples. Each data set was tested for normality using the Shapiro-Wilks test before assuming Gaussian distribution and equal standard deviations and proceeding with the analysis (unless otherwise stated). One-way ANOVA (mean of treatments compared to controls) and Dunnett's test for multiple comparisons were used to determine significance ($p<0.05$). Significant p values are shown in graphs as *$p<0.05$, **$p<0.01$, ***$p<0.001$, ****$p<0.0001$. All statistical analyses and graphs were performed and generated using GraphPad Prism 9.4.0.

5. Conclusions

The mechanisms regulating mitochondrial dynamics and their relationship to neuropathology are complex. Cell models provide a valuable approach to study these mechanisms and provide insight into understanding neurological disorders. Although gene and protein expression are common approaches to investigate these mechanisms in cell models, imaging techniques, specifically TEM, are an overlooked, valuable tool that directly visualizes endpoint mitochondrial morphology. SH-SY5Y cells treated with PPA showed altered mitochondrial morphology when visualized using TEM. These changes corresponded to decreased gene expression of the biogenesis genes, *NRF1* and *TFAM*, and the potential fusion gene, *STOML2*. Together, our data illustrate the utility of TEM to explore relationships between gene expression and mitochondrial morphology, inform more targeted mechanistic investigations and provide insight into the complexity of mitostasis in neurons.

Supplementary Materials: The following supporting information can be downloaded at: www.mdpi.com/xxx/s1 Table S1: Primer and probe sequences.

Author Contributions: Conceptualization, COR & EB; methodology, EB, SB, MJ, SM, CM & MvdW; software, CJ, EB; formal analysis, EB, CM, MvdW & CJ; resources, COR; data curation, EB & MJ; writing — original draft preparation, EB, CM, MvdW & COR; writing — reviewing and editing, all

authors; visualization, EB, MJ & CJ; supervision, COR; funding acquisition, COR. All authors have edited, read and agreed to the published version of the manuscript.

Funding: This research was funded by National Research Foundation, South Africa (Grant No. 138010). The role of CJ in this project has been made possible in part by grant number 2020-225445 from the Chan Zuckerberg Initiative DAF, an advised fund of Silicon Valley Community Foundation. The APC was partially funded by the University of Cape Town.

Institutional Review Board Statement: Not applicable.

Informed Consent Statement: Not applicable.

Data Availability Statement: The Fiji/ImageJ macros used for TEM image analysis are publicly available on GitHub here: https://github.com/caaja/TEMMitoMacro.

Acknowledgments: We would like to thank the National Research Foundation, South Africa for funding this research. We would like to thank the Electron Microscopy Unit (EMU), University Cape Town for the use of their facilities and Professor Bryan Trevor Sewell, Senior Scholar, Integrative Biomedical Sciences, University of Cape Town.

Conflicts of Interest: The authors declare no conflict of interest. The funders had no role in the design of the study; in the collection, analyses, or interpretation of data; in the writing of the manuscript; or in the decision to publish the results.

References

1. Meiliana, A.; Dewi, N.M.; Wijaya, A. Mitochondria: Master Regulator of Metabolism, Homeostasis, Stress, Aging and Epigenetics. *Indonesian Biomedical Journal* **2021**, *13*, 221–241, doi:10.18585/inabj.v13i3.1616.
2. Ben-Shachar, D. Mitochondrial Multifaceted Dysfunction in Schizophrenia; Complex I as a Possible Pathological Target. *Schizophr Res* **2017**, *187*, 3–10, doi:10.1016/j.schres.2016.10.022.
3. Bose, A.; Beal, M.F. Mitochondrial Dysfunction in Parkinson's Disease. *J Neurochem* **2016**, *139*, 216–231, doi:10.1111/jnc.13731.
4. Cai, Q.; Tammineni, P. Mitochondrial Aspects of Synaptic Dysfunction in Alzheimer's Disease. *Journal of Alzheimer's Disease* **2017**, *57*, 1087–1103, doi:10.3233/JAD-160726.
5. Guha, S.; Johnson, G.V.W.; Nehrke, K. The Crosstalk between Pathological Tau Phosphorylation and Mitochondrial Dysfunction as a Key to Understanding and Treating Alzheimer's Disease. *Mol Neurobiol* **2020**, *57*, 5103–5120, doi:10.1007/s12035-020-02084-0.
6. Guo, L.; Tian, J.; Du, H. Mitochondrial Dysfunction and Synaptic Transmission Failure in Alzheimer's Disease. *Journal of Alzheimer's Disease* 2017, *57*, 1071–1086.
7. Nabi, S.U.; Khan, A.; Siddiqui, E.M.; Rehman, M.U.; Alshahrani, S.; Arafah, A.; Mehan, S.; Alsaffar, R.M.; Alexiou, A.; Shen, B. Mechanisms of Mitochondrial Malfunction in Alzheimer's Disease: New Therapeutic Hope. *Oxid Med Cell Longev* **2022**, Article ID 4759963, doi:10.1155/2022/4759963.
8. Sharma, V.K.; Singh, T.G.; Mehta, V. Stressed Mitochondria: A Target to Intrude Alzheimer's Disease. *Mitochondrion* **2021**, *59*, 48–57, doi:10.1016/j.mito.2021.04.004.
9. Belenguer, P.; Duarte, J.M.N.; Schuck, P.F.; Ferreira, G.C. Mitochondria and the Brain: Bioenergetics and Beyond. *Neurotox Res* **2019**, *36*, 219–238, doi:10.1007/s12640-019-00061-7.
10. Rangaraju, V.; Lewis, T.L.; Hirabayashi, Y.; Bergami, M.; Motori, E.; Cartoni, R.; Kwon, S.K.; Courchet, J. Pleiotropic Mitochondria: The Influence of Mitochondria on Neuronal Development and Disease. *Journal of Neuroscience* **2019**, *39*, 8200–8208, doi:10.1523/JNEUROSCI.1157-19.2019.
11. Wang, Y.M.; Qiu, M.Y.; Liu, Q.; Tang, H.; Gu, H.F. Critical Role of Dysfunctional Mitochondria and Defective Mitophagy in Autism Spectrum Disorders. *Brain Res Bull* **2021**, *168*, 138–145, doi:10.1016/j.brainresbull.2020.12.022.
12. Khacho, M.; Clark, A.; Svoboda, D.S.; Azzi, J.; MacLaurin, J.G.; Meghaizel, C.; Sesaki, H.; Lagace, D.C.; Germain, M.; Harper, M.E.; et al. Mitochondrial Dynamics Impacts Stem Cell Identity and Fate Decisions by Regulating a Nuclear Transcriptional Program. *Cell Stem Cell* **2016**, *19*, 232–247, doi:10.1016/j.stem.2016.04.015.
13. Khacho, M.; Slack, R.S. Mitochondrial Dynamics in the Regulation of Neurogenesis: From Development to the Adult Brain. *Developmental Dynamics* **2018**, *247*, 47–53, doi:10.1002/dvdy.
14. Kyriakoudi, S.; Drousiotou, A.; Petrou, P.P. When the Balance Tips: Dysregulation of Mitochondrial Dynamics as a Culprit in Disease. *Int J Mol Sci* **2021**, *22*, 4617, doi:10.3390/ijms22094617.
15. Cardanho-Ramos, C.; Morais, V.A. Mitochondrial Biogenesis in Neurons: How and Where. *Int J Mol Sci* **2021**, *22*, 13059, doi:10.3390/ijms222313059.
16. Yu, R.; Lendahl, U.; Nistér, M.; Zhao, J. Regulation of Mammalian Mitochondrial Dynamics: Opportunities and Challenges. *Front Endocrinol (Lausanne)* **2020**, *11*, 374, doi:10.3389/fendo.2020.00374.

17. Rai, S.N.; Singh, C.; Singh, A.; Singh, M.P.; Singh, K.B. Mitochondrial Dysfunction: A Potential Therapeutic Target to Treat Alzheimer's Disease. *Mol Neurobiol* **2022**, *57*, 3075–3088, doi:10.1007/s12035-020-01945-y/Published.
18. Rani, L.; Mondal, A.C. Emerging Concepts of Mitochondrial Dysfunction in Parkinson's Disease Progression: Pathogenic and Therapeutic Implications. *Mitochondrion* **2020**, *50*, 25–34, doi:10.1016/j.mito.2019.09.010.
19. Collins, H.E.; Kane, M.S.; Litovsky, S.H.; Darley-Usmar, V.M.; Young, M.E.; Chatham, J.C.; Zhang, J. Mitochondrial Morphology and Mitophagy in Heart Diseases: Qualitative and Quantitative Analyses Using Transmission Electron Microscopy. *Frontiers in Aging* **2021**, *2*, doi:10.3389/fragi.2021.670267.
20. Wai, T.; Langer, T. Mitochondrial Dynamics and Metabolic Regulation. *Trends in Endocrinology and Metabolism* **2016**, *27*, 105–117, doi:10.1016/j.tem.2015.12.001.
21. Glancy, B. Visualizing Mitochondrial Form and Function within the Cell. *Trends Mol Med* 2020, *26*, 58–70.
22. Winey, M.; Meehl, J.B.; O'Toole, E.T.; Giddings Jr, T.H. Conventional Transmission Electron Microscopy. *Mol Biol Cell* **2014**, *25*, 319–323, doi:10.1091/mbc.E12-12-0863.
23. Paradis, M.; Kucharowski, N.; Edwards Faret, G.; José Maya Palacios, S.; Meyer, C.; Stümpges, B.; Jamitzky, I.; Kalinowski, J.; Thiele, C.; Bauer, R.; et al. The ER Protein Creld Regulates ER-Mitochondria Contact Dynamics and Respiratory Complex 1 Activity. *Sci Adv* **2022**, *8*, eabo0155.
24. Naia, L.; Pinho, C.M.; Dentoni, G.; Liu, J.; Leal, N.S.; Ferreira, D.M.S.; Schreiner, B.; Filadi, R.; Fão, L.; Connolly, N.M.C.; et al. Neuronal Cell-Based High-Throughput Screen for Enhancers of Mitochondrial Function Reveals Luteolin as a Modulator of Mitochondria-Endoplasmic Reticulum Coupling. *BMC Biol* **2021**, *19*, 57, doi:10.1186/s12915-021-00979-5.
25. Peng, W.; Wong, Y.C.; Krainc, D. Mitochondria-Lysosome Contacts Regulate Mitochondrial Ca 2+ Dynamics via Lysosomal TRPML1. *PNAS* **2020**, *117*, 19266–19275, doi:10.1073/pnas.2003236117.
26. Wong, Y.C.; Ysselstein, D.; Krainc, D. Mitochondria-Lysosome Contacts Regulate Mitochondrial Fission via RAB7 GTP Hydrolysis. *Nature* **2018**, *554*, 382–386, doi:10.1038/nature25486.
27. Shipley, M.M.; Mangold, C.A.; Szpara, M.L. Differentiation of the SH-SY5Y Human Neuroblastoma Cell Line. *Journal of Visualized Experiments* **2016**, 53193, doi:10.3791/53193.
28. Capetian, P.; Müller, L.; Volkmann, J.; Heckmann, M.; Ergün, S.; Wagner, N. Visualizing the Synaptic and Cellular Ultrastructure in Neurons Differentiated from Human Induced Neural Stem Cells—an Optimized Protocol. *Int J Mol Sci* **2020**, *21*, 1708, doi:10.3390/ijms21051708.
29. Merrill, R.A.; Flippo, K.H.; Strack, S. Measuring Mitochondrial Shape with ImageJ. In *Techniques to Investigate Mitochondrial Function in Neurons.*; Strack, S., Usachev, Y., Eds.; Humana Press: New York, NY, 2017; Vol. 123, pp. 31–48 ISBN 9781493968909.
30. Lam, J.; Katti, P.; Biete, M.; Mungai, M.; Ashshareef, S.; Neikirk, K.; Lopez, E.G.; Vue, Z.; Christensen, T.A.; Beasley, H.K.; et al. A Universal Approach to Analyzing Transmission Electron Microscopy with ImageJ. *Cells* **2021**, *10*, 2177, doi:10.3390/cells10092177.
31. Abdelli, L.S.; Samsam, A.; Naser, S.A. Propionic Acid Induces Gliosis and Neuro-Inflammation through Modulation of PTEN/AKT Pathway in Autism Spectrum Disorder. *Sci Rep* **2019**, *9*, 8824, doi:10.1038/s41598-019-45348-z.
32. Choi, H.; Kim, I.S.; Mun, J.Y. Propionic Acid Induces Dendritic Spine Loss by MAPK/ERK Signaling and Dysregulation of Autophagic Flux. *Mol Brain* **2020**, *13*, 86, doi:10.1186/s13041-020-00626-0.
33. Jung, M.; Choi, H.; Kim, J.; Mun, J.Y. Correlative Light and Transmission Electron Microscopy Showed Details of Mitophagy by Mitochondria Quality Control in Propionic Acid Treated SH-SH5Y Cell. *Materials* **2020**, *13*, 4336, doi:10.3390/ma13194336.
34. Kim, S.A.; Jang, E.H.; Mun, J.Y.; Choi, H. Propionic Acid Induces Mitochondrial Dysfunction and Affects Gene Expression for Mitochondria Biogenesis and Neuronal Differentiation in SH-SY5Y Cell Line. *Neurotoxicology* **2019**, *75*, 116–122, doi:10.1016/j.neuro.2019.09.009.
35. Ostendorf, F.; Metzdorf, J.; Gold, R.; Haghikia, A.; Tönges, L. Propionic Acid and Fasudil as Treatment against Rotenone Toxicity in an in Vitro Model of Parkinson's Disease. *Molecules* **2020**, *25*, 2502, doi:10.3390/molecules25112502.
36. Alfawaz, H.A.; El-Ansary, A.; Al-Ayadhi, L.; Bhat, R.S.; Hassan, W.M. Protective Effects of Bee Pollen on Multiple Propionic Acid-Induced Biochemical Autistic Features in a Rat Model. *Metabolites* **2022**, *12*, 571, doi:10.3390/metabo12070571.
37. Al-Ghamdi, M.; Al-Ayadhi, L.; El-Ansary, A. Selected Biomarkers as Predictive Tools in Testing Efficacy of Melatonin and Coenzyme Q on Propionic Acid - Induced Neurotoxicity in Rodent Model of Autism. *BMC Neurosci* **2014**, *15*, 34, doi:10.1186/1471-2202-15-34.
38. Choi, J.; Lee, S.; Won, J.; Jin, Y.; Hong, Y.; Hur, T.Y.; Kim, J.H.; Lee, S.R.; Hong, Y. Pathophysiological and Neurobehavioral Characteristics of a Propionic Acid-Mediated Autism-like Rat Model. *PLoS One* **2018**, *13*, e0192925, doi:10.1371/journal.pone.0192925.
39. El-Ansary, A.K.; Bacha, A.B.; Kotb, M. Etiology of Autistic Features: The Persisting Neurotoxic Effects of Propionic Acid. *J Neuroinflammation* **2012**, *9*, 174, doi:10.1186/1742-2094-9-74.
40. Macfabe, D.F.; Rodríguez-Capote, K.; Hoffman, J.E.; Franklin, A.E.; Mohammad-Asef, Y.; Taylor, A.R.; Boon, F.; Cain, D.P.; Kavaliers, M.; Possmayer, F.; et al. A Novel Rodent Model of Autism: Intraventricular Infusions of Propionic Acid

Increase Locomotor Activity and Induce Neuroinflammation and Oxidative Stress in Discrete Regions of Adult Rat Brain. *Am J Biochem Biotechnol* **2008**, *4*, 146–166, doi:https://doi.org/10.3844/ajbbsp.2008.146.166.

41. Özkul, B.; Urfalı, F.E.; Sever, İ.H.; Bozkurt, M.F.; Söğüt, İ.; Elgörmüş, Ç.S.; Erdogan, M.A.; Erbaş, O. Demonstration of Ameliorating Effect of Vardenafil through Its Anti-Inflammatory and Neuroprotective Properties in Autism Spectrum Disorder Induced by Propionic Acid on Rat Model. *International Journal of Neuroscience* **2022**, *132*, 1150–1164, doi:10.1080/00207454.2022.2079507.
42. Shultz, S.R.; MacFabe, D.F.; Ossenkopp, K.P.; Scratch, S.; Whelan, J.; Taylor, R.; Cain, D.P. Intracerebroventricular Injection of Propionic Acid, an Enteric Bacterial Metabolic End-Product, Impairs Social Behavior in the Rat: Implications for an Animal Model of Autism. *Neuropharmacology* **2008**, *54*, 901–911, doi:10.1016/j.neuropharm.2008.01.013.
43. Mirza, R.; Sharma, B. A Selective Peroxisome Proliferator-Activated Receptor-γ Agonist Benefited Propionic Acid Induced Autism-like Behavioral Phenotypes in Rats by Attenuation of Neuroinflammation and Oxidative Stress. *Chem Biol Interact* **2019**, *311*, 108758, doi:10.1016/j.cbi.2019.108758.
44. Khera, R.; Mehan, S.; Bhalla, S.; Kumar, S.; Alshammari, A.; Alharbi, M.; Sadhu, S.S. Guggulsterone Mediated JAK/STAT and PPAR-Gamma Modulation Prevents Neurobehavioral and Neurochemical Abnormalities in Propionic Acid-Induced Experimental Model of Autism. *Molecules* **2022**, *27*, 889, doi:10.3390/molecules27030889.
45. Giddings, T.H. Freeze-Substitution Protocols for Improved Visualization of Membranes in High-Pressure Frozen Samples. *J Microsc* **2003**, *212*, 53–61, doi:https://doi.org/10.1046/j.1365-2818.2003.01228.x.
46. Hawes, P.; Netherton, C.L.; Mueller, M.; Wileman, T.; Monaghan, P. Rapid Freeze-Substitution Preserves Membranes in High-Pressure Frozen Tissue Culture Cells. *J Microsc* **2007**, *226*, 182–189, doi:10.1111/j.1365-2818.2007.01767.x.
47. Frye, R.E.; Lionnard, L.; Singh, I.; Karim, M.A.; Chajra, H.; Frechet, M.; Kissa, K.; Racine, V.; Ammanamanchi, A.; McCarty, P.J.; et al. Mitochondrial Morphology Is Associated with Respiratory Chain Uncoupling in Autism Spectrum Disorder. *Transl Psychiatry* **2021**, *11*, 1–17, doi:10.1038/s41398-021-01647-6.
48. Johnson, J.; Mercado-Ayon, E.; Mercado-Ayon, Y.; Dong, Y.N.; Halawani, S.; Ngaba, L.; Lynch, D.R. Mitochondrial Dysfunction in the Development and Progression of Neurodegenerative Diseases. *Arch Biochem Biophys* 2021, *702*, 108698.
49. Balachandar, V.; Rajagopalan, K.; Jayaramayya, K.; Jeevanandam, M.; Iyer, M. Mitochondrial Dysfunction: A Hidden Trigger of Autism? *Genes Dis* **2021**, *8*, 629–639, doi:10.1016/j.gendis.2020.07.002.
50. Frye, R.E.; Rose, S.; Chacko, J.; Wynne, R.; Bennuri, S.C.; Slattery, J.C.; Tippett, M.; Delhey, L.; Melnyk, S.; Kahler, S.G.; et al. Modulation of Mitochondrial Function by the Microbiome Metabolite Propionic Acid in Autism and Control Cell Lines. *Transl Psychiatry* **2016**, *6*, e927, doi:10.1038/tp.2016.189.
51. Stathopoulos, S.; Gaujoux, R.; Lindeque, Z.; Mahony, C.; van der Colff, R.; van der Westhuizen, F.; O'Ryan, C. DNA Methylation Associated with Mitochondrial Dysfunction in a South African Autism Spectrum Disorder Cohort. *Autism Research* **2020**, *13*, 1079–1093, doi:10.1002/aur.2310.
52. Jin, Z.; Liu, Y. DNA Methylation in Human Diseases. *Genes Dis* **2018**, *5*, 1–8, doi:10.1016/j.gendis.2018.01.002.
53. Ehrlich, M. DNA Hypermethylation in Disease: Mechanisms and Clinical Relevance. *Epigenetics* **2019**, *14*, 1141–1163, doi:10.1080/15592294.2019.1638701.
54. Desviat, L.R.; Pérez, B.; Pérez-Cerdá, C.; Rodríguez-Pombo, P.; Clavero, S.; Ugarte, M. Propionic Acidemia: Mutation Update and Functional and Structural Effects of the Variant Alleles. *Mol Genet Metab* **2004**, *83*, 28–37, doi:10.1016/j.ymgme.2004.08.001.
55. Shahmoradian, S.H.; Galiano, M.R.; Wu, C.; Chen, S.; Rasband, M.N.; Mobley, W.C.; Chiu, W. Preparation of Primary Neurons for Visualizing Neurites in a Frozen-Hydrated State Using Cryo-Electron Tomography. *Journal of Visualized Experiments* **2014**, *84*, e50783, doi:10.3791/50783.
56. Fu, W.; Liu, Y.; Yin, H. Mitochondrial Dynamics: Biogenesis, Fission, Fusion, and Mitophagy in the Regulation of Stem Cell Behaviors. *Stem Cells Int* **2019**, *2019*, Article ID: 9757201, doi:10.1155/2019/9757201.
57. Fillier, T.A.; Shah, S.; Doody, K.M.; Pham, T.H.; Aubry, I.; Tremblay, M.L.; Cheema, S.K.; Blundell, J.; Thomas, R.H. Brief Exposure of Neuronal Cells to Levels of SCFAs Observed in Human Systemic Circulation Impair Lipid Metabolism Resulting in Apoptosis. *Sci Rep* **2022**, *12*, 14355, doi:10.1038/s41598-022-18363-w.
58. Gambini, E.; Martinelli, I.; Stadiotti, I.; Vinci, M.C.; Scopece, A.; Eramo, L.; Sommariva, E.; Resta, J.; Benaouadi, S.; Cogliati, E.; et al. Differences in Mitochondrial Membrane Potential Identify Distinct Populations of Human Cardiac Mesenchymal Progenitor Cells. *Int J Mol Sci* **2020**, *21*, 7467, doi:10.3390/ijms21207467.
59. Tang, Y.; Chen, Y.; Jiang, H.; Nie, D. Short-Chain Fatty Acids Induced Autophagy Serves as an Adaptive Strategy for Retarding Mitochondria-Mediated Apoptotic Cell Death. *Cell Death Differ* **2011**, *18*, 602–618, doi:10.1038/cdd.2010.117.
60. Tondera, D.; Grandemange, S.; Jourdain, A.; Karbowski, M.; Mattenberger, Y.; Herzig, S.; da Cruz, S.; Clerc, P.; Raschke, I.; Merkwirth, C.; et al. SLP-2 Is Required for Stress-Induced Mitochondrial Hyperfusion. *EMBO Journal* **2009**, *28*, 1589–1600, doi:10.1038/emboj.2009.89.
61. Otera, H.; Miyata, N.; Kuge, O.; Mihara, K. Drp1-Dependent Mitochondrial Fission via MiD49/51 Is Essential for Apoptotic Cristae Remodeling. *Journal of Cell Biology* **2016**, *212*, 531–544, doi:10.1083/jcb.201508099.

62. Chen, H.; Detmer, S.A.; Ewald, A.J.; Griffin, E.E.; Fraser, S.E.; Chan, D.C. Mitofusins Mfn1 and Mfn2 Coordinately Regulate Mitochondrial Fusion and Are Essential for Embryonic Development. *J Cell Biol* **2003**, *160*, 189–200, doi:10.1083/jcb.200211046.
63. Bam, S.; Buchanan, E.; Mahony, C.; O'Ryan, C. DNA Methylation of PGC-1α Is Associated with Elevated MtDNA Copy Number and Altered Urinary Metabolites in Autism Spectrum Disorder. *Front Cell Dev Biol* **2021**, *9*, 696428, doi:10.3389/fcell.2021.696428.
64. Anitha, A.; Nakamura, K.; Thanseem, I.; Matsuzaki, H.; Miyachi, T.; Tsujii, M.; Iwata, Y.; Suzuki, K.; Sugiyama, T.; Mori, N. Downregulation of the Expression of Mitochondrial Electron Transport Complex Genes in Autism Brains. *Brain Pathology* **2013**, *23*, 294–302, doi:10.1111/bpa.12002.
65. Tang, G.; Rios, P.G.; Kuo, S.-H.; Akman, H.O.; Rosoklija, G.; Tanji, K.; Dwork, A.; Schon, E.A.; DiMauro, S.; Goldman, J.; et al. Mitochondrial Abnormalities in Temporal Lobe of Autistic Brain. *Neurobiol Dis* **2013**, *54*, 349–361, doi:10.1016/j.nbd.2013.01.006.
66. Pecorelli, A.; Ferrara, F.; Messano, N.; Cordone, V.; Schiavone, M.L.; Cervellati, F.; Woodby, B.; Cervellati, C.; Hayek, J.; Valacchi, G. Alterations of Mitochondrial Bioenergetics, Dynamics, and Morphology Support the Theory of Oxidative Damage Involvement in Autism Spectrum Disorder. *The FASEB Journal* **2020**, *34*, 6521–6538, doi:10.1096/fj.201902677r.
67. Carrasco, M.; Salazar, C.; Tiznado, W.; Ruiz, L.M. Alterations of Mitochondrial Biology in the Oral Mucosa of Chilean Children with Autism Spectrum Disorder (ASD). *Cells* **2019**, *8*, 367, doi:10.3390/cells8040367.
68. van der Bliek, A.M.; Shen, Q.; Kawajiri, S. Mechanisms of Mitochondrial Fission and Fusion. *Cold Spring Harb Perspect Biol* **2013**, *5*, a011072, doi:10.1101/cshperspect.a011072.
69. Benard, G.; Karbowski, M. Mitochondrial Fusion and Division: Regulation and Role in Cell Viability. *Semin Cell Dev Biol* **2009**, *20*, 365–374, doi:10.1016/j.semcdb.2008.12.012.
70. Xie, L.; Shi, F.; Li, Y.; Li, W.; Yu, X.; Zhao, L.; Zhou, M.; Hu, J.; Luo, X.; Tang, M.; et al. Drp1-Dependent Remodeling of Mitochondrial Morphology Triggered by EBV-LMP1 Increases Cisplatin Resistance. *Signal Transduct Target Ther* **2020**, *5*, 56, doi:10.1038/s41392-020-0151-9.
71. Zhu, P.P.; Patterson, A.; Stadler, J.; Seeburg, D.P.; Sheng, M.; Blackstone, C. Intra- and Intermolecular Domain Interactions of the C-Terminal GTPase Effector Domain of the Multimeric Dynamin-like GTPase Drp1. *Journal of Biological Chemistry* **2004**, *279*, 35967–35974, doi:10.1074/jbc.M404105200.
72. Christie, D.A.; Mitsopoulos, P.; Blagih, J.; Dunn, S.D.; St-Pierre, J.; Jones, R.G.; Hatch, G.M.; Madrenas, J. Stomatin-like Protein 2 Deficiency in T Cells Is Associated with Altered Mitochondrial Respiration and Defective CD4 + T Cell Responses. *The Journal of Immunology* **2012**, *189*, 4349–4360, doi:10.4049/jimmunol.1103829.
73. Mitsopoulos, P.; Chang, Y.-H.; Wai, T.; König, T.; Dunn, S.D.; Langer, T.; Madrenas, J. Stomatin-like Protein 2 Is Required for in Vivo Mitochondrial Respiratory Chain Supercomplex Formation and Optimal Cell Function. *Mol Cell Biol* **2015**, *35*, 1838–1847, doi:10.1128/mcb.00047-15.
74. Qu, H.; Jiang, W.; Wang, Y.; Chen, P. Stoml2 as a Novel Prognostic Biomarker Modulates Cell Proliferation, Motility and Chemo-Sensitivity via IL6-Stat3 Pathway in Head and Neck Squamous Cell Carcinoma. *Am J Transl Res* **2019**, *11*, 683–695.
75. Zheng, Y.; Huang, C.; Lu, L.; Yu, K.; Zhao, J.; Chen, M.; Liu, L.; Sun, Q.; Lin, Z.; Zheng, J.; et al. STOML2 Potentiates Metastasis of Hepatocellular Carcinoma by Promoting PINK1-Mediated Mitophagy and Regulates Sensitivity to Lenvatinib. *J Hematol Oncol* **2021**, *14*, 16, doi:10.1186/s13045-020-01029-3.
76. Qin, C.; Wang, Y.; Zhao, B.; Li, Z.; Li, T.; Yang, X.; Zhao, Y.; Wang, W. STOML2 Restricts Mitophagy and Increases Chemosensitivity in Pancreatic Cancer through Stabilizing PARL-Induced PINK1 Degradation. *Preprint available at Research Square* **2022**, doi:https://doi.org/10.21203/rs.3.rs-1952708/v1.
77. Hájek, P.; Chomyn, A.; Attardi, G. Identification of a Novel Mitochondrial Complex Containing Mitofusin 2 and Stomatin-like Protein 2. *Journal of Biological Chemistry* **2007**, *282*, 5670–5681, doi:10.1074/jbc.M608168200.
78. Schindelin, J.; Arganda-Carreras, I.; Frise, E.; Kaynig, V.; Longair, M.; Pietzsch, T.; Preibisch, S.; Rueden, C.; Saalfeld, S.; Schmid, B.; et al. Fiji: An Open-Source Platform for Biological-Image Analysis. *Nat Methods* **2012**, *9*, 676–682, doi:10.1038/nmeth.2019.
79. Ansari, N.; Müller, S.; Stelzer, E.H.K.; Pampaloni, F. Quantitative 3D Cell-Based Assay Performed with Cellular Spheroids and Fluorescence Microscopy. In *Methods in Cell Biology*; Michael Conn, M.P., Ed.; Academic Press, 2013; Vol. 113, pp. 295–309.
80. Kosmider, B.; Lin, C.R.; Karim, L.; Tomar, D.; Vlasenko, L.; Marchetti, N.; Bolla, S.; Madesh, M.; Criner, G.J.; Bahmed, K. Mitochondrial Dysfunction in Human Primary Alveolar Type II Cells in Emphysema. *EBioMedicine* **2019**, *46*, 305–316, doi:10.1016/j.ebiom.2019.07.063.
81. Duraisamy, A.J.; Mohammad, G.; Kowluru, R.A. Mitochondrial Fusion and Maintenance of Mitochondrial Homeostasis in Diabetic Retinopathy. *BBA - Molecular Basis of Disease* **2019**, *1865*, 1617–1626, doi:10.1016/j.bbadis.2019.03.013.
82. Schrier, M.S.; Zhang, Y.; Trivedi, M.S.; Deth, R.C. Decreased Cortical Nrf2 Gene Expression in Autism and Its Relationship to Thiol and Cobalamin Status. *Biochimie* **2022**, *192*, 1–12, doi:10.1016/j.biochi.2021.09.006.

83. Pinho, S.A.; Costa, C.F.; Deus, C.M.; Pinho, S.L.C.; Miranda-Santos, I.; Afonso, G.; Bagshaw, O.; Stuart, J.A.; Oliveira, P.J.; Cunha-Oliveira, T. Mitochondrial and Metabolic Remodelling in Human Skin Fibroblasts in Response to Glucose Availability. *FEBS Journal* **2022**, *289*, 5198–5217, doi:10.1111/febs.16413.
84. Ye, P.; Li, W.; Huang, X.; Zhao, S.; Chen, W.; Xia, Y.; Yu, W.; Rao, T.; Ning, J.; Zhou, X.; et al. BMAL1 Regulates Mitochondrial Homeostasis in Renal Ischaemia-Reperfusion Injury by Mediating the SIRT1/PGC-1α Axis. *J Cell Mol Med* **2022**, *26*, 1994–2009, doi:10.1111/jcmm.17223.
85. Hu, G.; Zhang, J.; Xu, F.; Deng, H.; Zhang, W.; Kang, S.; Liang, W. Stomatin-like Protein 2 Inhibits Cisplatin-Induced Apoptosis through MEK/ERK Signaling and the Mitochondrial Apoptosis Pathway in Cervical Cancer Cells. *Cancer Sci* **2018**, *109*, 1357–1368, doi:10.1111/cas.13563.
86. Grady, J.P.; Murphy, J.L.; Blakely, E.L.; Haller, R.G.; Taylor, R.W.; Turnbull, D.M.; Tuppen, H.A.L. Accurate Measurement of Mitochondrial DNA Deletion Level and Copy Number Differences in Human Skeletal Muscle. *PLoS One* **2014**, *9*, e114462, doi:10.1371/journal.pone.0114462.
87. Livak, K.J.; Schmittgen, T.D. Analysis of Relative Gene Expression Data Using Real-Time Quantitative PCR and the 2-$\Delta\Delta$CT Method. *Methods* **2001**, *25*, 402–408, doi:10.1006/meth.2001.1262.